

1 Earthquakes triggered by the subsurface undrained response to reservoir- 2 impoundment at Irapé, Brazil

3 Haris Raza^{1,2,3*}, George Sand França^{1,2}, Eveline Sayão¹, Victor Vilarrasa³

4 ¹Seismological Observatory, Graduate Program in Geology, Institute of Geosciences, University of Brasília,
5 Campus Darcy Ribeiro, 70297-400 Brasília, Brazil

6 ²Institute of Astronomy, Geophysics and Atmospheric Sciences, University of São Paulo, 05508-090, São
7 Paulo, Brazil

8 ³Global Change Research Group (GCRG), IMEDEA, CSIC-UIB, 07190 Esporles, Spain

9 *Correspondence to: Haris Raza (harisraza90@yahoo.com), Victor Vilarrasa (victor.vilarrasa@csic.es)

10 Abstract

11 The necessity to reduce carbon emissions to mitigate climate change is accelerating the transition from fossil
12 fuels to renewable energy sources. Specifically, hydropower has emerged as a prominent and safe renewable
13 energy source, but entails reservoir-triggered seismicity (RTS). This phenomenon causes significant
14 challenges for safe reservoir management. Irapé, in Brazil, is a prominent RTS site where seismicity surged
15 after reservoir filling, with a maximum event of magnitude 3.0 in May 2006, just six months after the start of
16 reservoir impoundment. Despite more than a decade has passed since the seismicity occurred, the factors
17 governing these earthquakes and their connection to subsurface rock properties remain poorly understood.
18 Here, we attempt to understand the potential causes of RTS at Irapé dam, which is the highest dam in Brazil
19 with 208 m, and the second highest in South America. Permeability and porosity measurements of cylindrical
20 cores from hard and intact rock samples which have been extracted near the RTS zone, by pitting 10 cm from
21 the surface reveal a low-permeability rock. Porosity values range from 6.3 to 14.7%. Only three out of the
22 eleven tested samples present permeability above the lowest measurable value of the apparatus (0.002 mD),
23 with the highest permeability being 0.0098 mD. The undrained response of the low-permeability rock placed
24 below the reservoir results in an instantaneous increase in pore pressure and poroelastic stress changes due to
25 elastic compression, which brings potential faults located below the reservoir closer to failure conditions.
26 According to our analytical calculations, the vertical loading caused by the increase in 136 m of the reservoir-
27 water level caused lead to a 0.61 MPa pore pressure buildup in response to compression at the depth of the
28 Magnitude 3.0 earthquake, i.e., 3.88 km, resulting in an increase of 0.75 MPa in the vertical effective stress

29 and of 0.48 MPa in the horizontal effective stress. These changes resulted in an increase in the deviatoric stress
30 that led to fault destabilization, causing the RTS. The laboratory measurements and analytical calculations
31 corroborate the hypothesis that the initial seismic activity was induced by the undrained subsurface response
32 to the reservoir loading at Irapé.

33 **Keywords:** Brazil, Reservoir-triggered seismicity, Permeability, Porosity, Fault, Reservoir-management

34 **1.Introduction**

35 Reservoir impoundment, deep underground mining, and fluid injection into and withdrawal from the
36 subsurface are some of the well-known causes of induced/triggered seismicity which have become a global
37 issue in the past few decades (McGarr et al., 2002; Foulger et al., 2018; Kivi et al., 2023). The understanding
38 and identification of these types of human-induced earthquakes is crucial in terms of environmental and
39 economic impact, as well as for socio-political and scientific discussion (Gonzalez et al., 2012; Vilarrasa et
40 al., 2019). Recently, the debate over potential induced or triggered nature of cases of felt seismicity has
41 intensified, such as the Oklahoma earthquakes of Mw 5.7 in 2011 and of Mw 5.8 in 2016 (Ellsworth, 2013;
42 Keranen et al., 2013; Yeck et al., 2017), Emilia, Italy, earthquakes of Mw 6.1 and 5.9 in 2012 (Cesca et al.,
43 2013a), Pohang, South Korea, earthquake of Mw 5.5 in 2017 (Grigoli et al., 2018; Kim et al., 2018), Lorca,
44 Spain, earthquake of Mw 5.1 in 2011 (González et al., 2012), and Castor, Spain, earthquake sequence of Mw
45 4.1 in 2013 (Cesca et al., 2014; Vilarrasa et al., 2021; Vilarrasa et al., 2022), to name a few. Apart from the
46 possibility of injuring people and damaging infrastructure, such earthquakes can have a negative public
47 perception leading to project cancellation (Boyet et al., 2023a).

48 The first reservoir-triggered seismicity (RTS) case was observed during the filling of Lake Mead at the
49 Hoover Reservoir (US) in the mid-1930s, with ~M4.0 (Carder 1945). Major worldwide RTS cases were
50 detected in the 1960s, such as the M6.1 Hsinenghiang (China) in 1962, Kariba (Zambia) M6.2 in 1963,
51 Kremasta (Greece) M6.3 in 1966, and Koyna (India) M6.3 in 1967 (Gupta, 2002). To date, over 150 RTS
52 cases have been documented (Wilson et al., 2017; Foulger et al., 2018). Studies to understand the triggering
53 mechanisms of RTS show that pore pressure changes in the order of a few tenth of MPa and the associated

54 poroelastic stress changes are sufficient to reactivate deep faults (Rice and Cleary, 1976; Simpson, 1976; Bell
 55 and Nur, 1978; Talwani and Acree, 1985; Roeloffs, 1988; Simpson et al., 1988).

56 RTS is generally controlled by the stress state, the geological and hydrogeological properties of the region,
 57 and the water-level changes at the reservoir. The perturbation caused by the changes in water-level results in
 58 the loading and/or unloading of the subsurface, which may respond in an undrained or drained way. An
 59 undrained response leads to an instantaneous pore pressure buildup that is proportional to the height of the
 60 reservoir load. In contrast, a drained response leads to pore pressure diffusion into the rock that causes
 61 progressive pore pressure build-up as the pressure front propagates into the rock (Table 1). In general, RTS
 62 magnitudes are smaller for undrained responses than drained ones (Simpson et al., 1988). The interactions and
 63 comprehensive analysis of these two responses are key to understand the causes of RTS cases and eventually
 64 improve the forecasting and mitigation of RTS hazard.

65 **Table 1.** The time-distribution types of responses to reservoir-triggered earthquakes (by Simpson, 1988)

Response type	Mechanism	Description	Main features	Cases
Instantaneous response	Instantaneous elastic response and undrained response due to reservoir loading	This type of RTS increases immediately after the initial impoundment of reservoir or changes rapidly after rapid changes in the water level.	Changes in water level have a strong correlation with the change of seismicity, this generally occurs around the reservoir area, and the earthquake magnitude is small, the majority of them are swarm seismicity.	Koyna, Monticello, Manico-3, Nurek, Kariba, Kremesta <i>Irapé (this paper)</i>
Delayed response	Increase of pore pressure caused by pressure diffusion through permeable rock below the reservoir	It is only after a period of reservoir impoundment that the seismicity changes continuously	No significant correlation between changes in water level and seismicity, the time delay is obvious, the magnitude is generally large, and the earthquake occurrence point is not limited.	Koyna, Aswan, Oroville

66
 67 The RTS cases are booming around the world, with Brazil being one of the concerned countries with 29 RTS
 68 cases to date (Sayão et al., 2020). The study of RTS in Brazil started in 1972 with the M3.7 at Carmo do
 69 Cajuru reservoir, southeast Brazil (Foulger et al., 2018). The largest recorded event, a M4.2 in 1974, caused

70 damage to several buildings without any fatalities and was associated with nearby reservoirs at Porto
71 Colombia and Volta Grande, both of which started damming in the early 1970s (Sayão et al., 2020).

72 The Irapé dam, located in the state of Minas Gerais, Brazil, is the highest dam in Brazil with about 208 m,
73 and the second highest in South America (França et al., 2010). The Irapé hydropower plant lies in the vicinity
74 of Jequitinhonha River. Seismicity started to increase immediately after the impoundment of the reservoir and
75 completion of the dam with the maximum event of M3.0 occurred on 14 May 2006, coinciding with the peak
76 water level of the dam. The significant magnitude of the earthquake and the early occurrence after-filling of
77 the reservoir impoundment has raised questions about the triggering mechanisms of this RTS. Understanding
78 these mechanisms is crucial for ensuring the safety of infrastructure around the Irapé reservoir and for the
79 local population.

80 In this study, we aim to investigate the potential causes of the main RTS event at Irapé. We initially elaborate
81 on the geological setting and rock characteristics in the vicinity of the reservoir. We explain the characteristics
82 of the RTS at Irapé, including the temporal evolution of the seismicity, which occurred in the short period
83 from December 2005 to May 2006 and the location of the main event based on the local velocity model. Then,
84 we present the performed permeability and porosity tests of cylindrical cores from hard and intact rock
85 samples, which have been extracted near the RTS zone to identify and describe the primary role of porosity
86 and permeability. We perform analytical calculations to estimate the pore pressure and poroelastic stresses in
87 response to the highest water level of the reservoir filling and the time it would take for the pore pressure
88 diffusion front to reach the depth of the main event. We present evidence that the cause of RTS at Irapé was
89 the undrained response of the subsurface to reservoir impoundment.

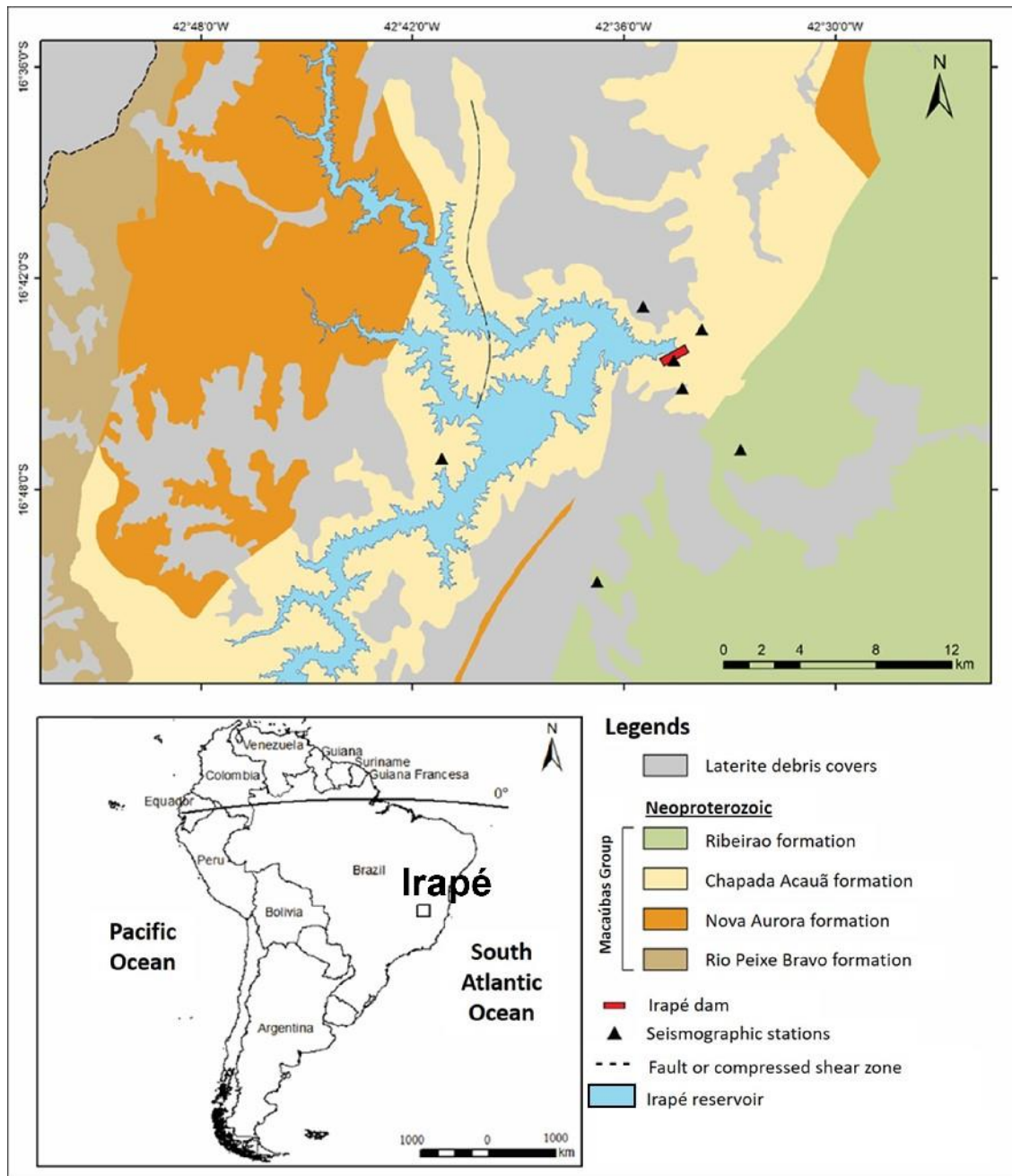
90 **2. Geological setting and RTS at Irapé**

91 **2.1 Geological setting**

92 The area of Irapé is located within the domain of the Pre-Folding Belt Cambrian Araçuaí, which is oriented
93 approximately in a north-south direction and defines the eastern part of the São Francisco Craton in the State
94 of Minas Gerais (Almeida, 1977). Approximately 80% of the reservoir area in Irapé corresponds to the

95 Chapada Acauã Formation. The Chapada Acauã Formation, which has been investigated near the Irapé Shear
96 Zone (Araujo et al., 2010), consists of carbonaceous mica-schist rocks, locally with pyrite, garnet, or graphite
97 (Lima, 2002). This rock is intensely deformed, characterized by the formation and rotation of quartz sub-
98 grains and the migration of grain edges (Araujo et al., 2010). This formation is characterized by typical passive
99 margin sedimentation and is associated with sediment deposition in the Macaúbas Basin along with the Nova
100 Aurora Formation (Silva et al., 2014). The Ribeirão da Folha Formation is found to the east of the Chapada
101 Acauã formation, consisting of mica shales, quartzite, and cal-silicates rock (Figure 1).

102



103

104 **Figure 1.** Geological map of Irapé reservoir and surrounding area

105 **2.2 Background on the reservoir-triggered seismicity at Irapé**

106 The Irapé reservoir covers an area of 137.8 km² with a reservoir volume of 5.964 km³. The dam was
 107 constructed on the Jequitinhonha River, filling the reservoir to a maximum height of 137 meters (Figure 1 and
 108 Table 2). The dam area was monitored by a three-component seismic network at three stations prior to three

109 years of its impoundment, which started on 7 December 2005. These stations did not detect any seismicity
 110 before the impoundment (Chimpliganond et al., 2007).

111 **Table 2.** Characteristics of the main RTS event at Irapé (França et al., 2010)

Dam height (m)	Length (m)	Volume (km ³)	Max. reservoir water depth (m)	Reservoir area (km ²)	Seismicity type	Date	Magnitude (mR)	Io (MMI)	ΔT (yr)
208	540	5.964	137	137.8	Initial	14 May 2006	3.0	III-IV	0.5

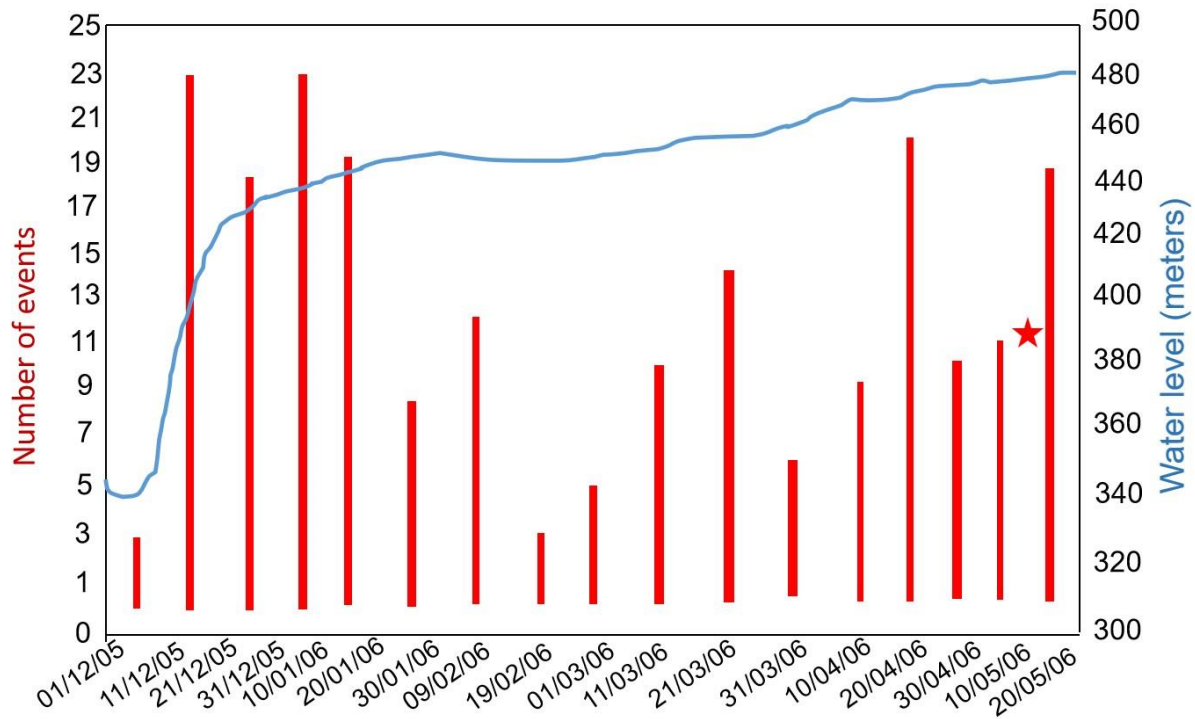
112 *ΔT : interval time (years) since the start of filling/impoundment; MMI: modified Mercalli Intensity*
 113 *scale, mR: magnitude Regional.*

114 Microearthquakes started to be detected just one day after the impoundment began, exceeding 300
 115 microearthquakes by October 2006. The largest event occurred on 14 May 2006 with a M3.0 that was felt at
 116 the reservoir area at a depth of 3.88 km (Chimpliganond et al., 2007; França et al., 2010). The seismicity
 117 occurred within a small area, with epicentres in the lake and its nearby margins (less than 3 km from the
 118 narrow lake), close to the dam axis. The epicenters are distributed from 0 to 11.4-km depth, showing a
 119 progressive increase in depth (see Table S1). The evident temporal correlation between the start of the
 120 reservoir impoundment and the occurrence of seismicity leads us to investigate a causative relationship
 121 (Figures 2 and 3). The spatial distribution of the epicentres also suggests the hypothesis that this is another
 122 case of RTS of the initial response type.

123

124

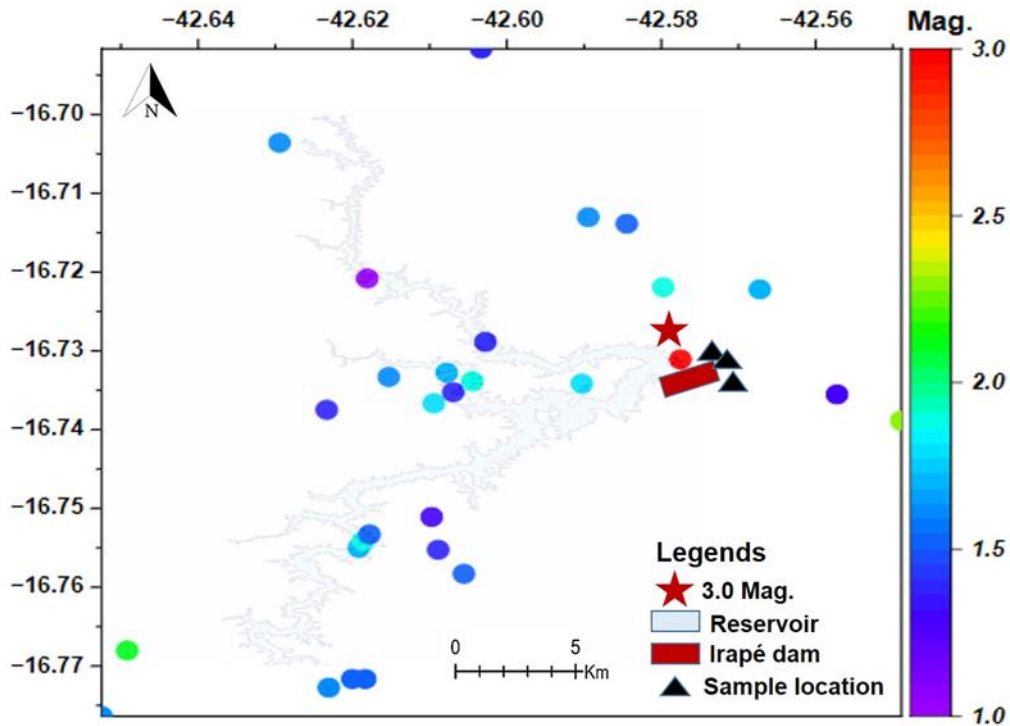
125



126

127 **Figure 2.** Temporal evolution of RTS at Irapé by ten days. Number of events during December 2005 to May
 128 2006 (histogram) at Irapé and average water elevation above the mean sea level (blue line) are illustrated. The
 129 red star indicates the time when the main and largest event occurred, M3.0 on 14 May 2006 (modified from
 130 Silva et al., 2014).

131 The events were analysed using the program Seismic Analysis Code (Goldstein and Snoke, 2005), in which
 132 the arrival of the P and S waves and the polarity are considered. The hypocentre location of the events that
 133 were recorded by three stations was computed with the program HYPO71 (Lee and Lahr, 1975). The analysis
 134 of seismograms went through a double-checks routine (Silva et al., 2014). The local monitoring station
 135 presented operational challenges, which resulted in positional uncertainty of seismic events (Silva et al.,
 136 2014). The velocity model that was used to locate the seismic events was based on a deep seismic refraction
 137 survey in combination with local geological interpretations and studies of the crustal structure in south-eastern
 138 Brazil (Assumpção et al., 2002b).



139

140 **Figure 3.** RTS Distribution in the initial period with location and magnitude (see colour scale), the red star is
 141 the main event felt near the dam and black triangles denote the samples location.

142 Velocity models were adopted based on a deep seismic refraction survey in combination with local
 143 geological interpretations and studies of the crustal structure in south-eastern Brazil to locate seismic events
 144 in the Irapé area (Assumpção et al., 2012). The local velocity model consists of a superficial 4.8 km-thick
 145 layer with a P-wave velocity (V_p) of 4.5 km/s, representing the mica-schist to graphite-schist rocks from
 146 surface, and a second layer from schist to crystalline basement rocks with a thickness of 11.2 km with P-wave
 147 velocity (V_p) of 6 km/s (Marshak et al., 2006; Silva et al., 2014).

148 The repetition of a structural trend in the NE-SW direction originates from the geological and geophysical
 149 structuring of the crust (Silva et al., 2014). The stress regime in the Irapé region has been estimated to be a
 150 normal faulting stress regime. The accuracy of the focal mechanisms remains a subject of debate due to the
 151 low quality of the seismic data recorded by analogue seismograms and uncertainties associated with the
 152 velocity model. Consequently, the focal mechanisms of the May 14, 2006, M3.0 earthquake have not been
 153 resolved yet (Silva et al., 2014).

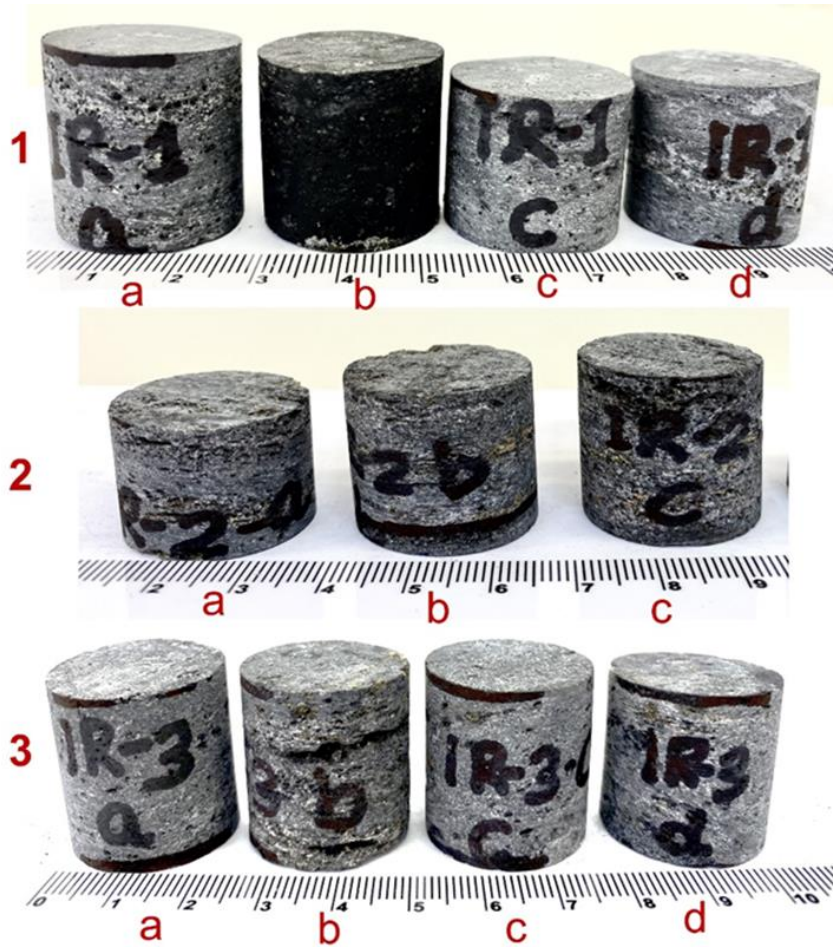
154 **3. Materials and methodology**

155 We inspected the Irapé site and surrounding areas as well as the outcrops. The dam area is surrounded by
156 mica-schist rock, which is shiny, ranging from blackish to medium grey in colour, with foliated, fine to
157 medium-grained textures. According to the local velocity model, there is a superficial layer that is 4.8-km
158 thick, representing mica-schist to graphite-schist rocks at the surface. Below that, there is a second layer that
159 is 11.2-km thick, consisting of crystalline basement rock. Measurements from these samples are crucial for
160 understanding the estimated permeability beneath the subsurface in the context of the main event, which
161 occurred at a depth of 3.88 km (França et al., 2010). Since the epicenter of the main event was located about
162 1 km away from the dam, we collected bulk rock samples from different locations around the dam, as well as
163 nearby outcrops, by digging pits that were 0.10-m deep.

164 **3.1 Laboratory experiments**

165 We have extracted cylindrical core samples perpendicular to the bedding planes of mica-schist rock. We
166 have performed tests on three sets of samples, with a total of 11 core samples, of hard and intact samples
167 because the rest of the samples were fragile and fractured during the coring from bulk samples (Table 3). The
168 retrieved cylindrical plugs have a length ranging from 3.8 to 5.0 cm and a diameter of 2.50 cm, which meets
169 the International standard criteria (Core Lab) to measure core plug samples by Ultra-Pore 300 and Ultra-Perm
170 610 (Figures 4).

171



172

173 **Figure 4.** The three sets of mica-schist rock samples (1, 2, and 3) after cylindrical coring from bulk samples
174 (\perp coring of cylindrical plugs has been done by loading perpendicular to the bedding planes).

175 We conduct porosity measurements using the Ultra-Pore 300, which is manufactured by Core Lab Instruments
176 in Texas, USA. The Ultra-Pore 300 is a gas expansion helium pycnometer specifically designed for
177 determining the grain volume or pore volume of both core plug and full-diameter samples. To achieve this,
178 we utilized matrix cups designed for samples with diameters ranging from 2.5 to 3.8 cm, equipped with a
179 Setra 204 transducer rated for pressures ranging from 0 to 1.72 MPa. We determined the pore volume using
180 the nitrogen gas (N_2) expansion technique (API,1998; Ceia et al., 2019).

181 We measure the intrinsic permeability of rock samples using Ultra-Perm 610 Permeameter. This precision
182 equipment, which controls backpressure, maintains a constant rate or mean pressure at 0.69 MPa. Before
183 testing, samples are cleaned with soxhlet equipment and toluene, followed by drying in an oven. The

184 permeability measurements included a permeameter, nitrogen source, stopwatch, a core holder, a bubble tube,
185 and a digital calliper. The core holder is pressurized to 3.45 MPa confining pressure using compressed air.
186 The bubbles passing through a burette are timed, and outflow gas volume is recorded. The permeability is
187 calculated using Darcy's law, considering core dimensions. Hard rock core samples, like mica-schist, require
188 long stabilization times due to the low permeability.

189 **3.2 Analytical calculations of undrained pore pressure and stress changes**

190 Reservoir impoundment causes an undrained effect in the subsurface that manifests as instantaneous pore
191 pressure and stress changes below the reservoir (Skempton, 1954). The change in the vertical stress, $\Delta\sigma_v$,
192 equals the weight of the water level rise assuming an extensive reservoir. The horizontal stress, assuming
193 oedometric conditions, changes because of the increase in the vertical stress and the undrained pore pressure
194 change as (Rutqvist, 2012)

195

$$196 \quad \Delta\sigma_h = \frac{\nu}{(1-\nu)} (\Delta\sigma_v) + \alpha \frac{(1-2\nu)}{(1-\nu)} \Delta p \quad (1)$$

191 where $\Delta\sigma_h$ is the horizontal stress change, α is Biot's coefficient, ν is Poisson's ratio and Δp is the pore
 192 pressure change. Additionally, in an isotropic and homogeneous poroelastic material subject to un-
 193 drained conditions, the change in pore pressure resulting from a change in stress can be computed as
 194 (e.g., Rice and Cleary, 1976; Cocco and Rice, 2002)

$$195 \quad \Delta p = \frac{B}{3} \Delta\sigma_{kk}, \quad (2)$$

196 where $\Delta\sigma_{kk} = \Delta\sigma_v + 2\Delta\sigma_h$, $\Delta\sigma_{kk}$ is the mean stress change and B is the Skempton's coefficient of
 197 mica-schist rock (Roeloffs, 1988). Here we adopt the sign criterion of geomechanics, i.e., compressive
 198 stresses are positive. Equations (1) and (2) constitute a system of two equations with two unknowns. Its
 199 resolution yields the undrained pore pressure change as

$$200 \quad \Delta p = \frac{B}{3} \frac{(1+\nu)\Delta\sigma_v}{\left(1-\nu-\frac{2B}{3}(\alpha-\nu-2\alpha\nu)\right)} \quad (3)$$

201 **3.3 Analytical calculations of the time at which the pore pressure diffusion front reaches the** 202 **depth of the earthquake**

203 The advancement of the pore pressure front within the subsurface is controlled by diffusivity

$$204 \quad D = \frac{k\rho g}{\mu S_s} \quad (4)$$

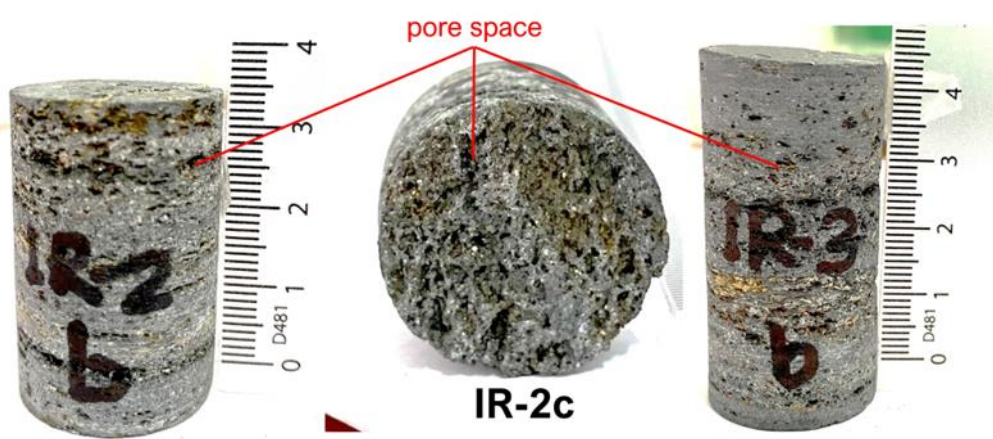
205 where, D is diffusivity, k is the intrinsic permeability, ρ is water density, g is gravity, μ is water viscosity,
 206 and S_s is the specific storage coefficient. The time at which the pore pressure front reaches a certain
 207 distance r is given by

$$208 \quad t = \frac{r^2}{D} \quad (5)$$

209 **4.Results**

210 **4.1 Porosity and permeability measurements**

211 The results of our laboratory measurements are provided in Table 3. These data are subject to meas-
 212 urement uncertainties inherent to the experimental equipment used according to the standard procedure.
 213 Laboratory measurements of samples of mica-schist reveal a low permeability (Table 3 and Figure 6).
 214 The maximum permeability is 0.0098 mD, but most of the samples present a permeability lowest meas-
 215 urable value of the apparatus, i.e., 0.002 mD. Such permeability is in the range of low-permeability
 216 rock, which act as a barrier to flow. Most of the samples have a porosity between 6 to 10%, except for
 217 two with higher porosity. The low permeability of mica-schist could be explained by the fact that the
 218 larger pores are not well connected (Figure 5). In general, there is no correlation between permeability
 219 and porosity (Figure 6).



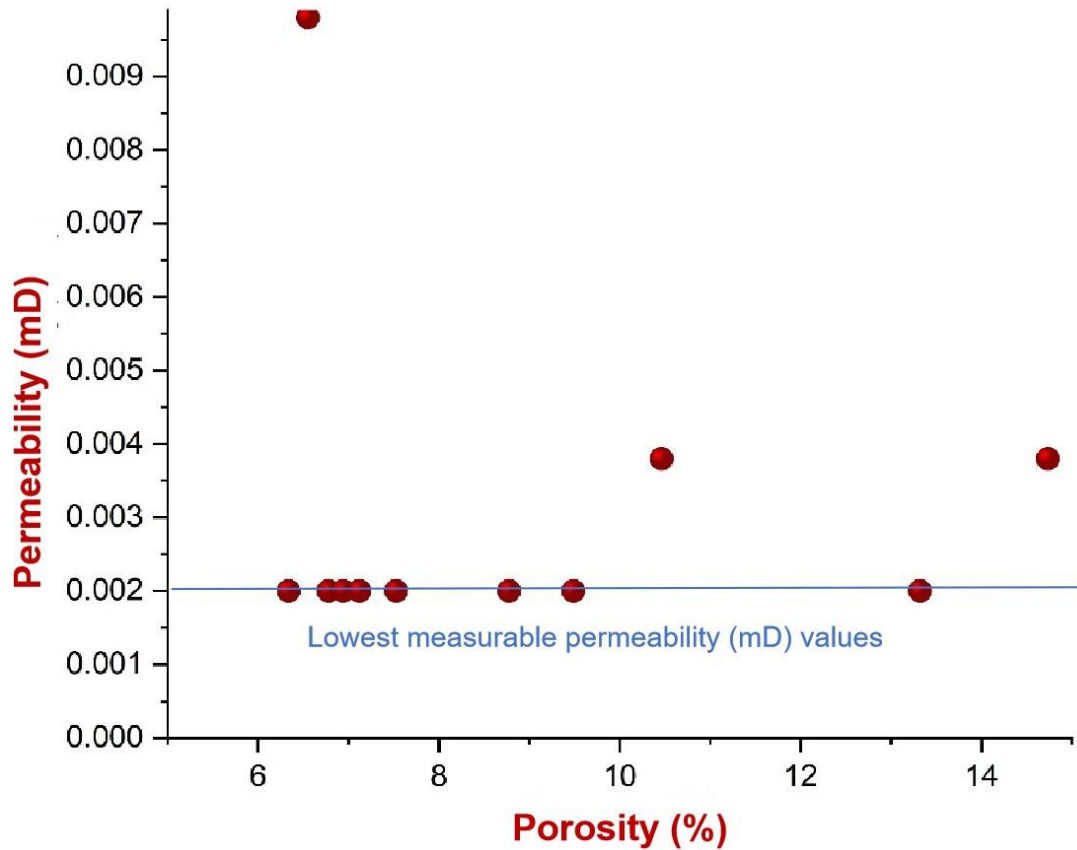
220
 221 **Figure 5.** Megascopic representation of samples IR-2 b, c, and IR-3b showing pores that are not well-
 222 connected.

223 **Table 3.** Location of samples with permeability and porosity data from measured cores

224

Location (lat., long.)	Sample Numbers	Permeability (mD)	Porosity (%)
16.73872, 42.57680	IR-1a	<0.002	7.5
	IR-1b	<0.002	6.8
	IR-1c	<0.002	8.8
	IR-1d	0.0098	6.6
16.74038, 42.57652	IR-2a	<0.002	9.5
	IR-2b	0.0038	10.5
	IR-2c	0.0038	14.7
16.72438, 42.56316	IR-3a	<0.002	6.9
	IR-3b	<0.002	13.3
	IR-3c	<0.002	7.1
	IR-3d	<0.002	6.3

225 *Experiments loaded perpendicular to bedding plane (\perp)*



226

227 **Figure 6.** Porosity-permeability relation of mica-schist rock samples.

228 **4.2 Undrained response of rock: changes in pore pressure and stress**

229 The 136 m of water level increase at the time of the M3.0 earthquake resulted in an increase in the
 230 vertical stress of 1.36 MPa. To compute the pore pressure change caused by the reservoir impoundment,
 231 the Biot coefficient, Skempton’s B coefficient and Poisson’s ratio of mica-schist are needed (Eq. (3)).
 232 Since such measurements are not available, we adopt the values of Opalinus Clay because it is a similar
 233 rock to mica-schist (both are shales primarily composed of quartz minerals). Thus, we assume
 234 Skempton’s B coefficient of 0.92, undrained Poisson’s ratio of 0.39 and Biot’s coefficient of 1. With
 235 these values, the resulting pore pressure change is 0.61 MPa. Consequently, the horizontal stress change
 236 is of 1.09 MPa (Eq. (1)). These pore pressure and stress changes result in an increase in the vertical
 237 effective stress of 0.75 MPa and in the horizontal effective stress of 0.48 MPa, increasing the deviatoric
 238 stress in more than 0.25 MPa.

239 **4.3 Pressure diffusion along mica-schist**

240 The measured intrinsic permeability of mica-schist is in the order of 10^{-18} m^2 (Table 3). Assuming a
241 specific storage coefficient in the order of $1.05 \times 10^{-6} \text{ m}^{-1}$, diffusivity (Eq. (4)) results in $9.5 \times 10^{-6} \text{ m}^2/\text{s}$.
242 Taking into account that the depth of the M3.0 earthquake occurred at 3.8 km, the time at which the
243 pore pressure front would reach this depth by diffusion (Eq. (5)) is in the order of 50,000 years by
244 assuming the absence of fractures.

245 **5. Discussion**

246 RTS has been the focus of many studies, but the origin and development of RTS are still unclear in
247 many cases (Gupta et al., 2016; Arora et al., 2018). There is a general consensus that there are two main
248 triggering mechanisms (Simpson et al., 1988). On the one hand, low-permeability rock has an undrained
249 response to the water-level changes of the reservoir, which acts as a loading, instantaneously increasing
250 pore pressure and causing poroelastic stress changes deep underground (Chen and Talwani, 2001;
251 Vilarrasa et al., 2022; Raza et al., 2023). On the other hand, in the presence of permeable rock or a
252 permeable fracture network, pore pressure diffuses downwards, which may eventually trigger an
253 earthquake if a critically stressed fault becomes pressurized (Talwani and Acree, 1985).

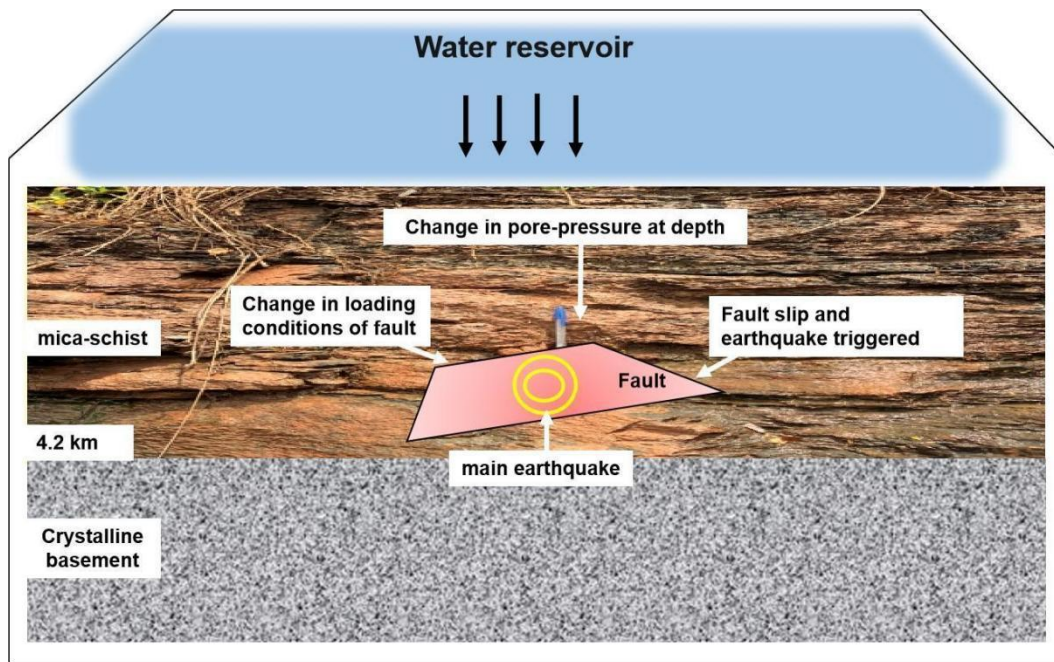
254 At Irapé, the low-permeability of the rock below the reservoir, i.e., mica-schist with permeability in
255 the order of 10^{-18} m^2 or lower, hinders pore pressure diffusion. Given that the hypocentre was located at
256 3.88 km depth, the pressure propagation front would take in the order of 50,000 years to start
257 pressurizing the depth at which the earthquake was nucleated. Even assuming that the presence of
258 fractures enhanced the rock permeability by three orders of magnitude, which would be the upper limit
259 of observed permeability enhancement of low-permeability rock at the field scale (Neuzil, 1986), the
260 pressure front would take 50 years to reach 3.88 km depth. The permeability enhancement due to the
261 presence of fractures could become larger in crystalline than in clay-rich rock, reaching an increase of
262 up to five orders of magnitude (Bondarenko et al., 2022). Such high permeability enhancement caused
263 by fractures is not feasible in clay-rich rock like mica-schist because of its ductility and low dilatancy
264 angle, which prevents fractures from becoming open pathways. At Irapé, the necessary permeability of
265 the rock to reach the depth of the largest earthquake within 0.5 years, i.e., the delay of the earthquake
266 with respect to the start of impoundment, would be of 10^{-13} m^2 , five orders of magnitude higher than

267 the actual permeability of mica-schist. Such high permeability enhancement is deemed unlikely for
268 mica-schist.

269 Considering the load caused by the water-level rise in the reservoir of 136 m, the low-permeability
270 mica-schist experienced an undrained response, with subsequent poroelastic stress and pore water
271 changes. We have estimated these changes analytically, finding a vertical effective stress increase of
272 0.75 MPa, a horizontal effective stress increase of 0.48 MPa, and a pore pressure increase of 0.61 MPa.
273 Given the normal faulting stress regime at Irapé, these changes cause an increase in the deviatoric stress
274 that could destabilize faults in the subsurface. These changes in pore pressure and stress levels provide
275 valuable insights into the dynamic behaviour of the geological formation and are crucial considerations
276 in understanding the reservoir response to alterations in reservoir water levels. We contend that the rapid
277 loading of the reservoir weakens this fault because of the undrained stress and pore pressure changes
278 (Figure 7).

279 In addition, the megascopic representation of core samples in the configuration of the physical
280 evidence illustrates that rock can exhibit relatively high porosities and low permeability when their
281 pores are not well-connected (Figure 5). Thus, mica-schist may present preferential lateral fluid
282 migration at depth, following the foliation direction. The surface rock beneath the Irapé reservoir is
283 highly metamorphosed and despite having high porosity, the rock presents low permeability. Therefore,
284 pore pressure diffusion is disregarded as the potential cause triggering the seismicity at Irapé.

285



286

287 **Figure 7.** Schematic description of the mechanism of RTS at Irapé, indicating the effect of the weight
 288 of the reservoir water volume due to undrained response in low-permeable mica-schist rock (the
 289 background photo was taken in the field from an outcrop at Irapé).

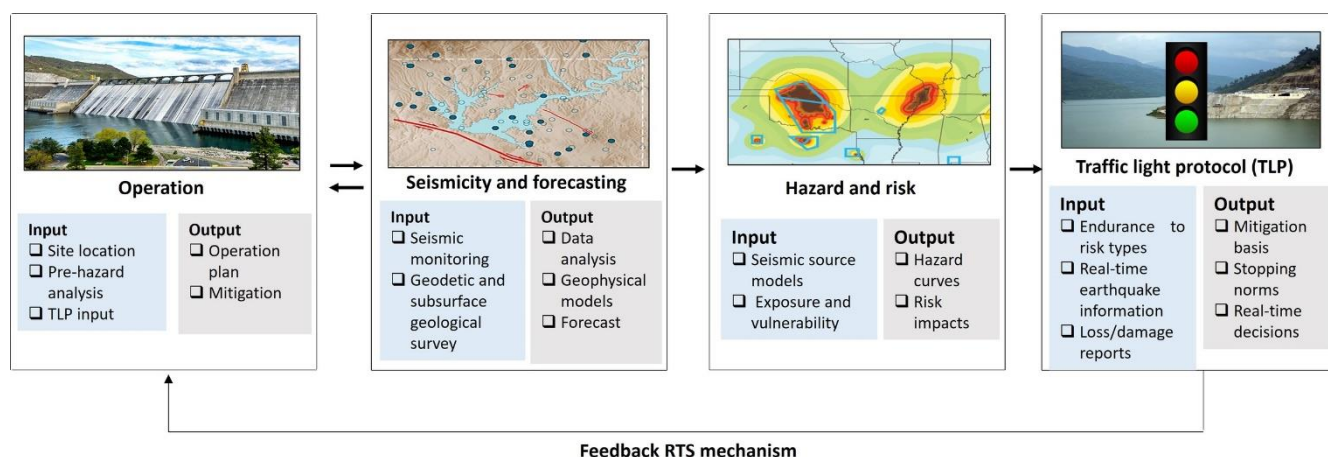
290 The regional geology at the eastern part of the São Francisco Craton in the State of Minas Gerais
 291 follows a N-S direction (Almeida, 1977). Silva et al. (2014) also mentioned that the repetition of a
 292 structural trend in the NE-SW direction originates from the geological and geophysical structuring of
 293 the crust. This trend makes it feasible to assume the existence of a N-S vertical mature fault that could
 294 become destabilized by small changes in the effective stress. An association of such seismicity with the
 295 shear zone along reservoir /lineaments suggests the reactivation of such faults under the influence of
 296 reservoir impoundment.

297 Mitigation of the risk of RTS requires knowledge of the physical mechanisms that may trigger
 298 seismicity. Thus, a thorough characterization of the site to measure rock physical properties is crucial.
 299 Analytical and numerical solutions should integrate the physics of the problem, in particular,
 300 poromechanics to assess both the undrained response of the subsurface to reservoir impoundment and
 301 pore-pressure diffusion. Such models should include the rock layers below the reservoir down to the
 302 crystalline basement and their characteristics, including features like faults. Before the construction of

303 the dam, the hazard of triggering moderate to large earthquakes should be estimated, to disregard
 304 locations with high probability of RTS. This estimation requires knowing the hydro-mechanical
 305 properties of the rock layers, i.e., permeability, porosity, stiffness, and strength, as well as the design
 306 parameters of the dam, i.e., height for potential future projects. Note that at Irapé, the porosity and
 307 permeability measurements have not been done until now, but should have been done prior to the design
 308 of the dam. The successful management of RTS requires an interdisciplinary approach combining
 309 concepts of hydrogeology, geomechanics and seismology.

310 To address and manage RTS risks, the Traffic Light Protocol (TLP) should be employed (Figure 8). A
 311 TLP is a tool that assists decision makers to decide how to operate the dam to minimize risks. The TLP
 312 has three levels of operation: (1) a green light that allows operations to proceed without restrictions, (2)
 313 a yellow light that requires to activate mitigation measures, and (3) a red light that urges to stop opera-
 314 tion Efforts have been made regarding the incorporation of real-time data with the application risk-
 315 oriented measures to prevent infrastructure damage and nuisance to the local community. Incorporating
 316 in TLP the two types of RTS, i.e., immediate events induced by the undrained response of the subsurface
 317 to water-level changes, and delayed seismicity induced by pore pressure diffusion, is crucial. To this
 318 end, the utilization of physics-based models is promising since they are capable of anticipating seismic
 319 activity, enabling operational adjustments for future mitigation of RTS risk (Boyet et al., 2023b) (Figure
 320 8).

321



322

323

324 **Figure 8.** Reservoir operations and impoundment are strategically designed to reduce the risk of RTS.

325 Monitoring seismic and geophysical activities yields information for predictive earthquake models. The

326 catalogues of earthquakes and source/origin models are applicable in the assessment of hazard and risk.

327 These assessments of risk and hazard can guide the development of a traffic light protocol (TLP), func-

328 tioning as a dynamic decision module during operations. The display of each box shows the classifica-

329 tions of input data (blue boxes) and output results (grey boxes).

330 Regarding the mitigation approaches for RTS within the framework of a TLP, the effectiveness of an

331 operator heavily relies on the efficiency of mitigation strategies implemented at the yellow-light stage.

332 Ideally, these strategies would proficiently diminish seismic risks and hazards, ultimately circumvent-

333 ing the red-light scenario that terminates the operation. Thus, TLPs can be one major strategy and strong

334 decision-making tool for operators to minimize the risk of RTS for future developments of dams.

335 **6.Conclusions**

336 We have analysed RTS at Irapé to discern the cause of the triggered seismicity. The measured low

337 permeability of the rock at Irapé disregards pore pressure diffusion as the triggering mechanism and

338 suggests that the M3.0 RTS was triggered by the undrained response of the subsurface to reservoir

339 impoundment. Analytical calculations estimate that pore pressure increased by 0.61 MPa in response

340 to an increase of 136 m in the reservoir-water level. The resulting vertical effective stress increased by

341 0.75 MPa and the horizontal effective stress by 0.48 MPa. Thus, the deviatoric stress would increase in

342 a normal faulting stress regime, like the one at Irapé, destabilizing the fault and causing RTS. Both

343 laboratory measurements and analytical calculations support the hypothesis that the initial seismicity

344 was triggered by the undrained response of the subsurface to the loading of the reservoir at Irapé. This

345 study suggests that the occurrence of such earthquakes may be avoided by thorough site characterization

346 and carefully management of the reservoir loading following TLPs that mitigate RTS risk.

347 **Data availability**

348 The data analysed and /or used in this study are presented in the Supplementary Material.

349 **Supplementary Material**

350 The Supplementary Material related to this article is available online.

351 **Author contributions**

352 H.R., G.S.F., V.V. co-designed the study. E.S. and H.R. did sample and provided map. H.R. wrote the
353 paper performed laboratory measurements. H.R. and V.V. did the analytical calculations. All authors
354 reviewed, contributed to the interpretation of the results, and edited the paper.

355 **Competing interests**

356 The corresponding and co-authors state that there are no competing interests.

357 **Acknowledgments**

358 This study was financed in part by the Coordenação de Aperfeiçoamento de Pessoal de Nível Superior
359 -Brasil (CAPES) -Finance Code 001. The authors acknowledge funding from the Spanish National
360 Research Council (CSIC) under the Program for Scientific Cooperation iCOOP+ through the Project
361 COOPA20414. V.V. acknowledges funding from the European Research Council (ERC) under the
362 European Union's Horizon 2020 Research and Innovation Program through the Starting Grant
363 GGeoREST (www.georest.eu) under Grant agreement No. 801809. IMEDEA is an accredited "Maria de
364 Maeztu excellence Unit" (Grant CEX2021-001198, funded by MICIU/AEI/ 10.13039/501100011033).
365 G.S.F gratefully acknowledges CNPq (Grant 310240/2020-4 PQ-1C). G.S.F., H.R. and E.S. also thank
366 to INCTET-CNPq (Institutos Nacionais de Ciência e Tecnologia de estudos tectônicos) Brazil. We thank
367 to Prof. Carlos Jorge de Abreu for conducting samples measurements at Laboratory of Physical
368 Properties of Rocks at the University of Brasília.

369 **References**

370 Almeida FFM, The São Francisco Craton. Brazilian Journal of Geosciences,7:349-364,1977
371 API, 1998. Recommend Practices for Core Analysis. RP40. American Petroleum Institute. 2nd Edition.

372 Araujo Filho, J. O; Silva, G. F; Lima, E. A. M; Ferreiera, V. N; Batista, O. C. A; Franca, G. S.
373 Mapeamento Geoestrutural da área de influência da Usina Hidrelétrica de Irapé, Grão Mogol,
374 MG. Anais do 45º Congresso Brasileiro de Geologia, Sociedade Brasileira de Geologia, 2010.

375 Arora, K., Srinu, Y., Gopinadh, D., Chadha, R.K., Raza, H., Mikhailov, V., Ponomarev, A., Kiseleva, E.
376 and Smirnov, V. Lineaments in Deccan Basalts: The Basement Connection in the Koyna–Warna
377 RTS Region. Bull. Seismol. Soc. Amer., v.108 (5), DOI: 10.1785/0120180011, 2018.

378 Assumpção, M., James, D., & Snoke, A., Crustal thicknesses in SE Brazilian Shield by receiver function
379 analysis: Implications for isostatic compensation. J. Geophys. Res., 107(B1). ,2002b

380 Assumpção, M; Feng, M; Tassara, A; Julia, J., Models of crustal thickness for South America from
381 seismic refraction, receiver functions and surface wave tomography. Tectonophysics, 609:82-
382 96, 2012.

383 Bell, M.L., Nur, A., Strength changes due to reservoir-induced pore pressure, stresses, and application
384 to Lake Oro-Berrocal. J. Geophys. Res. 83, 4469–4483, 1978.

385 Bondarenko, N., Podladchikov, Y. & Makhnenko, R. Hydromechanical impact of basement rock on
386 injection-induced seismicity in Illinois Basin. Sci Rep 12, 15639 .
387 <https://doi.org/10.1038/s41598-022-19775-4> (2022)

388 Boyet, A., De Simone, S., Ge, S. et al. Poroelastic stress relaxation, slip stress transfer and friction
389 weakening controlled post-injection seismicity at the Basel Enhanced Geothermal System.
390 Commun Earth Environ 4, 104. <https://doi.org/10.1038/s43247-023-00764-y> (2023).

391 Boyet, A., De Simone, S., Vilarrasa, V.; Physics-Based Modeling to Understand and to Propose
392 Forecasting Methods of Induced Seismicity. Seismological Research Letters ; 94 (6): 2666–
393 2678. doi: <https://doi.org/10.1785/0220230109>, 2023.

394 Carder, D. S. (1945). Seismic investigation in the Boulder Dam area, 1940-1944, and the influence of
395 reservoir loading on earthquake activity, Bull. Seism. Soc. Am. 35, 175-192.(1945).

396 Ceia Marco, Roseane Missagia, Ricardo Fasolo, Irineu Lima Neto, 2019. Relationship between
397 porosity, permeability, and pore compressibility; DOI: 10.22564/16cisbgf 2019.287, 2019

398 CEMIG - Minas Gerais Energy Company (2001). Geological observations in the UHE Irapé sector-
399 Consultancy Report. Belo Horizonte, MG, 6p, 2001

400 Cesca, S., Braun, T., Maccaferri, F., Passarelli, L., Rivalta, E., and Dahm, T. (2013a). Source modelling
401 of the M5–6 Emilia-Romagna, Italy, earthquakes (2012 May 20–29). *Geophys. J. Int.* 193,
402 1658–1672. doi: 10.1093/gji/ggt069, 2012.

403 Cesca, S., Grigoli, F., Heimann, S., González, Á, Buforn, E., Maghsoudi, S., et al. (2014). The 2013
404 September–October seismic sequence offshore Spain: a case of seismicity triggered by gas
405 injection? *Geophys. J. Int.* 198, 941–953. doi: 10.1093/gji/ggu172, 2014.

406 Chang, K.W., Yoon, H. Permeability-controlled migration of induced seismicity to deeper depths near
407 Venus in North Texas. *Sci Rep* 12, 1382 (2022). <https://doi.org/10.1038/s41598-022-05242-7>,
408 2022.

409 Chen, L., & Talwani, P. (2001). Mechanism of initial seismicity following impoundment of the
410 Monticello Reservoir, South Carolina. *Bulletin of the Seismological Society of America*, 91(6),
411 1582-1594, 2001.

412 Chimpliganond, C., G. S. França, A. E. Bandeira, and L. Bevilaqua (2007). Reservoir-triggered
413 seismicity at the highest Brazilian dam, AGU 2007 —Meeting of Americas Joint Assembly
414 Abstract, Acapulco, Mexico, Acapulco, Mexico, 22–25 May, 2007.

415 Cocco, M., Rice, J.M., 2002. Pore pressure and poroelasticity effects in Coulomb stress analysis of
416 earthquake interactions. *Journal of Geophysical Research* 107. doi:10.1029/2000JB000138,
417 2002.

418 Cornet, F. H., and J. Yin (1995), Analysis of induced seismicity for stress field determination and pore
419 pressure mapping, *Pure Appl. Geophysics.*, 145, 677–700, 1995.

420 CPRM - Mineral Resources Research Company (2004). Project Registration of Groundwater Supply
421 Sources. Jequitinhonha Valley: Diagnosis of the Municipality of Berilo-MG. Belo Horizonte,
422 43p, 2004.

423 Crane, L. J., & Friedman, A. (1956). The diffusion of chemically reacting systems in a laminar flow of
424 fluid. *AICHe Journal*, 2(2), 186-19, 1956.

425 *Developments in Structural Geology and Tectonics*, Elsevier, Volume 5, 2019, Pages 119-128,

426 Ellsworth, W. L. (2013). Injection-induced earthquakes. *Science* 341, 1225942. doi:
427 10.1126/science.1225942, 2013.

428 Foulger, G. R., Wilson, M., Gluyas, J., Julian, B. R., and Davies, R.: Global review of human-induced
429 earthquakes, *Earth-Sci. Rev.*, 178, 438–514, 2018.

430 França, G. S., Assumpção, M., Ribotta, L. C., Von Huelsen, M. G., and Chimpliganond, E. C. N.,
431 Updated compilation of reservoir triggered seismicity in Brazil, in 2010 The Meeting of the
432 Americas (AGU – American Geophysical Union), Foz do Iguaçu, Paraná, Brazil, 2010.

433 Golstein, P; Snoke, A. 2005. "Sac Availability for the Iris Community" Incorporated Institutions for
434 Seismology Data Management Center Eletronic Newsletter. Disponível em: Acessado em: 15
435 de dezembro de 2005.

436 González, P. J., Tiampo, K. F., Palano, M., Cannavó, F., and Fernández, J. (2012). The 2011 Lorca
437 earthquake slip distribution controlled by groundwater crustal unloading. *Nat. Geosci.* 5, 821–
438 825. doi: 10.1038/ngeo1610, 2012.

439 Gough, D.I., Gough, W.I., 1970a. Stress and deflection in the lithosphere near Lake Kariba, 1. *Geophys.*
440 *J. Int.* 21, 65–78, 1970a.

441 Golstein P. & Snoke A. 2005. "Sac Avaliability for the Iris Community" Incorporated Institutions for
442 Seismology Data Management Center Eletronic Newsletter. Disponível em:
443 www.iris.edu/news/newsletter/vol7no1/page1.htm. Acesso em: 15 dez 2013.

444 Gough, D.I., Gough, W.I., 1970b. Load-induced earthquakes at Kariba, 2. *Geophys. J. Int.* 21, 79–101,
445 1970b.

446 Grigoli, F., Cesca, S., Rinaldi, A. P., Manconi, A., López-Comino, J. A., Clinton, J. F., et al. (2018). The
447 November 2017 Mw 5.5 Pohang earthquake: a possible case of induced seismicity in South
448 Korea. *Science* 360, 1003–1006. doi: 10.1126/science.aat 2010, 2018.

449 Gupta, H. K., K. Arora, N. P. Rao, S. Roy, V. M. Tiwari, P. et al., Investigations of continued reservoir
450 triggered seismicity at Koyna, India, *Geol. Soc. Lond. Spec. Publ.* 445, 151–188 (2016).

451 Gupta, H. K.: A review of recent studies of triggered earthquakes by artificial water reservoirs with
452 special emphasis on earthquakes in Koyna, India, *Earth-Sci. Rev.* 58, 279–310,
453 [doi.org/10.1016/S0012-8252\(02\)00063-6](https://doi.org/10.1016/S0012-8252(02)00063-6), 2002.

454 Keranen, K. M., Savage, H. M., Abers, G. A., and Cochran, E. S. (2013). Potentially induced
455 earthquakes in Oklahoma, USA: Links between wastewater injection and the 2011 Mw 5.7
456 earthquake sequence. *Geology* 41, 699–702. doi: 10.1130/G34045., 2013.

457 Keranen, K. M., Weingarten, M., Abers, G. A., Bekins, B. A., and Ge, S. (2014). Sharp increase in
458 central Oklahoma seismicity since 2008 induced by massive wastewater injection. *Science* 345,
459 448–451. doi: 10.1126/science.1255802, 2014.

460 Kim, K.-H., Ree, J.-H., Kim, Y., Kim, S., Kang, S. Y., and Seo, W. (2018). Assessing whether the 2017
461 Mw 5.4 Pohang earthquake in South Korea was an induced event. *Science* 360, 1007–1009.
462 doi: 10.1126/science.aat6081, 2018.

463 Kivi, I. R., Boyet, A., Wu, H., Walter, L., Hanson-Hedgecock, S., Parisio, F., and Vilarrasa, V.: Global
464 physics-based database of injection-induced seismicity, *Earth Syst. Sci. Data*, 15, 3163–3182,
465 <https://doi.org/10.5194/essd-15-3163-2023>, 2023.

466 Lee, W. H. K.; Lahr, J. C., 1975. HYPO 1971 (revised a computer program for determining hypocentre,
467 magnitude and first motion pattern of local earthquakes. USGS, Open file report. 64 p., 1975.

468 Lima SAA, Martins-Neto MA, Predrosa-Soares AC, Cordani UG, Nutman A. 2002. The Salinas
469 Formation in the Type Area, NE of Minas Gerais: a proposal to review the stratigraphy of the
470 Araçuaí Belt based on sedimentary and metamorphic evidence and U-Pb SHRIMP ages.
471 *Brazilian Journal of Geosciences*, 34(4):491-500, 2002.

472 Marshak, S; Alkmim, F. F.; Whittington; Pedrosa-Soares, A. C. 2006. Extensional collapse in the
473 Neoproterozoic Araçuaí orogen, eastern Brazil: a setting for reactivation of asymmetric
474 crenulation cleavage. *Journal of Structural Geology*, 28(1):129-14, 2006.

475 McGarr, A., Simpson, D., and Seeber, L. (2002). 40—Case histories of induced and triggered seismicity.
476 *Int. Geophys.* 81A, 647–661, 2002.

477 Neuzil, C. E. (1986). Groundwater flow in low-permeability environments. *Water Resources Research*,
478 22(8), 1163-1195, 1986.

479 PLANVALE-Water Resources Master Plan for the Jequitinhonha and Pardo Valleys (1994). Diagnostic
480 Report carried out by Geotécnica and DHV Consultants BV, Annex B, Hydrogeology,
481 133p.,1994.

482 Raza, H., Kivi, I.R., França, G.S. and Vilarrasa V. Reservoir impoundment-triggered seismicity in
483 Brazil: the case of M4.0 Nova Ponte earthquake. *Sci Rep* 13, 22226 (2023).
484 <https://doi.org/10.1038/s41598-023-48924-6>, 2023.

485 Rice, J.R. and Cleary, M.P. (1976) Some basic stress-diffusion solutions for fluid-saturated elastic
486 porous media with compressible constituents. *Rev. Geophys. Space Phys.*, v.14, pp.227-241,
487 1976.

488 Roeloffs, E.A., 1988. Fault stability changes induced beneath a reservoir with cyclic variations in water
489 level. *J. Geophys. Res.* 93, 2107–212, 1988.

490 Rutqvist, J. (2012). The geomechanics of CO₂ storage in deep sedimentary formations. *Geotechnical
491 and Geological Engineering*, 30, 525-551, 2012.

492 Sausse, J., Fourar, M. and Genter, A. (2006) Permeability and alteration within the Soultz granite
493 inferred from geophysical and flow log analysis. *Geothermics*, v.35(5-6), pp.544-560, 2006.

494 Sayão, E., França, G. S., Holanda, M., and Gonçalves, A.: Spatial database and website for reservoir-
495 triggered seismicity in Brazil, *Nat. Hazards Earth Syst. Sci.*, 20, 2001–2019,
496 <https://doi.org/10.5194/nhess-20-2001-2020>, 2020.

497 Silva, G. F., J. O. Araújo Filho, M. G. Von Huelsen, C. N. Chimpliganond, and G. S. França (2014).
498 Influence of Brazilian structures on the reservoir-induced seismicity case of Irapé Hydroelectric
499 Plant, Minas Gerais, Brazil, *Braz. J. Geol.* 44, no. 3, 375–386, DOI: 10.5327/Z2317-
500 4889201400030004, 2014.

501 Simpson, D.W. (1976) Seismicity change associated with the reservoir loading. *Engg. Geol.*, v.10,
502 pp.123-150, 1976

503 Simpson, D.W., Leith, W.S. and Scholz, C.H. (1988) Two types of reservoirs induced seismicity. *Bull.
504 Seism. Soc. Amer.*, v.78, pp.2025–2040, 1988.

505 Simpson, DW 1986. Triggered Earthquakes. *Annual Review Earth Planetary Sciences*, 14: 21-42, 1986.

506 Skempton, A. W. (1954). The pore-pressure coefficients A and B. *Geotechnique*, 4(4), 143-14, 1954.

507 Snow, D.T., 1972. Geodynamics of seismic reservoirs. Proceedings of the Symposium on Percolation
508 through Fissured Rocks. Deutsche Gessellschaft für Erd- und Grundbau, Stuttgart, Germany,
509 pp. 1–19 (T2-J), 1972.

510 Talwani, P. and Acree, S. (1984/85), Pore pressure diffusion and mechanism of reservoir induced
511 seismicity. *Pure and applied Geophysics* 122,947-965, 1984/85.

512 Todd, D. K., & Mays, L. W. (2005). *Groundwater Hydrology*, 2005.

513 Vilarrasa, V., Carrera, J., Olivella, S., Rutqvist, J., and Laloui, L.: Induced seismicity in geologic carbon
514 storage, *Solid Earth*, 10, 871–892, <https://doi.org/10.5194/se-10-871-2019>, 2019.

515 Vilarrasa, V., De Simone, S., Carrera, J. et al. Multiple induced seismicity mechanisms at Castor
516 underground gas storage illustrate the need for thorough monitoring. *Nat. Commun.* 13, 3447
517 (2022). <https://doi.org/10.1038/s41467-022-30903-6>, 2022.

518 Vilarrasa, V., De Simone, S., Carrera, J., and Villaseñor, A.: Unravelling the causes of the seismicity
519 induced by underground gas storage at Castor, Spain, *Geophys. Res. Lett.*, 48, e2020GL092038,
520 <https://doi.org/10.1029/2020GL092038>, 2021.

521 Vilarrasa, V., Makhnenko, R. & Gheibi, S. 2016. Geomechanical analysis of the influence of CO₂
522 injection location on fault stability. *Journal of Rock Mechanics and Geotechnical Engineering*.
523 8(6):805–818, 2016.

524 Vilarrasa, V., Raza, H., Kivi, I. R., and França, G. S.: Understanding the triggering mechanisms of
525 reservoir-triggered seismicity at Nova Ponte, Brazil, through hydro-mechanical modeling, EGU
526 General Assembly 2023, Vienna, Austria, 24–28 Apr 2023, EGU23-11711,
527 <https://doi.org/10.5194/egusphere-egu23-11711>, 2023.

528 Wever, T. H. 1989. The Conrad discontinuity and the top of the reflective lower crust – do they coincide?
529 *Tectonophysics*,157:39-58, 1989.

530 Yeck, W. L., Weingarten, M., Benz, H. M., McNamara, D. E., Bergman, E. A., Herrmann, R. B., et al.
531 (2016). Far-field pressurization likely caused one of the largest injections induced earthquakes
532 by reactivating a large preexisting basement fault structure. *Geophys. Res. Lett.* 43, 10198–
533 10207. doi: 10.1002/2016GL07 0861, 2016.

534